Yang *et al. PhotoniX* (2025) 6:16
https://doi.org/10.1186/s43074-025-00174-7

PhotoniX

RESEARCH Open Access

Field programmable silicon microring WDM transceiver leveraging monolithically integrated phase-change materials

Xing Yang[1†], Shihuan Ran[1†], Ziquan Li[1], Liangjun Lu[1,2*], Yu Li[1,2*], Ngon Phu Wai[3], MingHua Zhang[3], Guo-Qiang Lo[3], Jianping Chen[1,2] and Linjie Zhou[1,2]

†Xing Yang and Shihuan Ran contributed equally to this work.

*Correspondence:
luliangjun@sjtu.edu.cn; yuli_seiee@sjtu.edu.cn

[1] State Key Laboratory of Advanced Optical Communication Systems and Networks, Department of Electronic Engineering, Shanghai Jiao Tong University, Shanghai 200240, China
[2] SJTU-Pinghu Institute of Intelligent Optoelectronics, Pinghu 314200, China
[3] Advanced Micro Foundry Pte Ltd., 11 Science Park Road, Singapore 117685, Singapore

Abstract

Silicon microring resonators (MRRs) with embedded PN junctions have emerged as pivotal components in high-capacity optical interconnects, serving as modulators or photodetectors due to their compact size, low power consumption, high bandwidth, and inherent wavelength selectivity. However, their resonance wavelengths are highly sensitive to fabrication-induced variations—nanometer-scale deviations in waveguide dimensions can result in significant resonance shifts—necessitating effective post-fabrication tuning mechanisms. Conventional solutions like integrating thermal phase shifters with MRRs enable wavelength tuning but at the cost of increased power consumption. Additionally, various wavelength trimming techniques including germanium ion implantation, continuous laser trimming, femtosecond laser trimming, and polymer material cladding, either have a limited tuning range or require a complex system, and hence they are not suitable for field programming of resonance wavelength. In this work, we introduce a novel integration of low-loss phase change material Sb_2Se_3 directly atop the PN junctions of silicon MRRs, enabling precise post-fabrication resonance trimming without altering the MRR physical dimensions or performance characteristics. By applying a forward-biased electrical pulse through the PN junction, we induce a phase transition in the Sb_2Se_3, achieving resonance wavelength tuning across an entire free spectral range (FSR) with minimal impact on modulation and detection capabilities and without the need for extra heating pads. We demonstrate the effectiveness of this method by uniformly aligning the resonance wavelengths of four cascaded SbSe-integrated MRRs, each capable of 100 Gbps on–off keying (OOK) modulation and detection, culminating in a combined data rate of 400 Gbps. Additionally, as enabled by such unique programmability, we propose a feedback scheme to counteract ambient temperature fluctuations as a real-time thermal management strategy during operation, employing one of the MRRs as an optical power monitor to stabilize the modulation of the remaining resonators. Via the non-volatile programmability, our approach significantly reduces static power consumption associated with wavelength adjustment. The use of a PN junction to trigger phase transition with forward-biased electrical pulses not only facilitates the in-situ wavelength trimming but also preserves the MRR perimeter with enough FSR to support the number of channels available for wavelength multiplexing. These advancements position Sb_2Se_3-integrated MRRs as a promising solution for large-scale, energy-efficient photonic transceivers in next-generation optical communication systems.

Keywords: Silicon photonics, Phase-change materials, Microring modulator, Photodetector

Introduction

The exponential growth of data center traffic driven by artificial intelligence, cloud computing, and the Internet of Things [1, 2] has intensified the demand for efficient optical interconnect solutions. Silicon photonics has emerged as a leading candidate due to its capacity for high-density integration and compatibility with complementary metal–oxide–semiconductor (CMOS) fabrication processes. Among silicon photonic devices, microring resonators (MRRs) embedded with PN junctions have garnered significant attention as modulators [3–5] and photodetectors (PDs) [6–8], owing to their compact footprint, enhanced power efficiency, and simplified fabrication that circumvents the need for germanium epitaxial growth. These advantages position MRRs favorably over Mach–Zehnder interferometer (MZI) modulators, silicon straight waveguide PDs [7, 9–16], and germanium PD [17], particularly for large-scale integration in next-generation high-density interconnects.

Despite their promising attributes, the commercialization of silicon MRRs faces substantial challenges, primarily due to their sensitivity to fabrication imperfections and environmental temperature fluctuations [18]. Minute deviations in fabrication can lead to significant shifts in the resonance wavelength, necessitating precise post-fabrication tuning mechanisms. Conventional approaches employ thermal phase shifters integrated atop the MRRs to align their resonance wavelengths with desired values [3, 4, 19–22]. However, this method incurs considerable static power consumption and contributes to thermal crosstalk—issues that become increasingly problematic as integration density rises.

To address these limitations, various non-volatile wavelength trimming techniques have been explored, aiming to permanently modify the effective refractive index of the waveguide. Methods such as germanium ion implantation [18, 23–25], continuous laser trimming [26–28], femtosecond laser trimming [29, 30], and polymer material cladding [31, 32] have been investigated. However, germanium ion implantation and continuous laser trimming can only induce index reductions, causing blue shifts in resonance that limit their practical utility. Femtosecond laser trimming offers both blue and red shifts by adjusting the irradiated fluence but necessitates the removal of the silica upper cladding and relies on complex optical systems, hindering in-situ trimming applications. Polymer cladding materials, while effective, generally lack compatibility with CMOS processes [31, 32]. Consequently, these methods fall short of providing flexible, reconfigurable, and non-volatile wavelength trimming suitable for MRR-based optical devices.

Recent years have witnessed significant interest in low-loss phase-change materials (PCMs) such as Sb_2Se_3 (SbSe) and Sb_2S_3 for photonic applications [33–38]. Unlike high-loss PCMs like $Ge_2Sb_2Te_5$ and $Ge_2Sb_2Se_4Te_1$, Sb_2Se_3 and Sb_2S_3 provide substantial refractive index modulation with minimal optical losses, making them ideal for pure phase modulation. Their non-volatile nature—maintaining their state without continuous voltage supply—further enhances their suitability for integrated photonic devices.

Phase transitions in these materials can be induced through hot-plate heating, free-space optical illumination, or on-chip local resistive heating via electrical pulses [39–41]. Notably, the integration of PCMs with micro-heaters based on graphene, indium tin oxide (ITO), doped silicon, and PIN diodes has been extensively explored for their controllability and scalability [40–48]. A non-volatile MZI switch integrated with SbSe for phase trimming has been demonstrated [49]. However, integrating a dedicated PIN junction into MRR-based modulators or PDs for phase transition introduces two critical design constraints. First, the additional PIN junction necessitates dedicated electrical pads for heating the PCM, increasing the overall chip area and electrical connection complexity. Second, the geometric expansion of the MRR perimeter caused by the PIN integration reduces the free spectral range (FSR) of the resonator, thereby limiting the achievable wavelength-division multiplexing (WDM) channels.

To address these issues, we propose a non-volatile MRR-based transceiver by integrating SbSe directly on the PN junction. This integration enables flexible resonance wavelength allocation and trimming by applying forward-biased electrical pulses to the PN junction to trigger phase transition. An aluminum oxide layer is inserted between the PN junction and the PCM to ensure that adjustments to the MRR resonance wavelength do not compromise its modulation and detection performance. We demonstrate an optical transceiver utilizing an array of four silicon MRRs with back-end integrated SbSe patches, achieving 4 × 100 Gbps on–off keying (OOK) modulation and detection across precisely aligned transmission channels, benefiting from the large tuning range of exceeding one FSR. Furthermore, we implement a stabilization scheme to maintain consistent MRR performance under ambient temperature variations. By employing an adjacent MRR as a power meter to monitor intracavity power and utilizing a thermoelectric cooler (TEC) for temperature control, we achieve stable modulation within the MRR array. Experimental results confirm that the SbSe-integrated MRRs operate reliably despite changes in environmental temperature.

This approach offers several advantages. Firstly, the utilization of the low-loss SbSe PCM for non-volatile resonance wavelength reconfiguration offers an efficient and flexible method for in-situ post-fabrication trimming of the MRR-based transceivers, solving the main bottleneck for the application of high-capacity high-density optical interconnects. Secondly, utilizing the positively biased PN junction—already used for modulation and detection—to induce the PCM phase change eliminates the need for additional heating pads and increased MRR perimeter, thus effectively reducing the chip area and maintaining the number of wavelength-multiplexed channels it can accommodate. Thirdly, the utilization of an adjacent MRR as an on-chip power monitor in the stabilization of the MRR array simplifies the feedback control system against environmental temperature fluctuation, especially for a large array number of integrated MRRs. This innovation provides a compelling solution for energy-efficient, high-density optical interconnects. Table 1 shows the comparison of our method with other post-fabrication trimming schemes. Our scheme can achieve resonance wavelength adjustment in both directions upon amorphization and crystallization processes, with an adjustment range exceeding one FSR, which is essential for non-volatile post-fabrication wavelength trimming. Additionally, the usage of ~ millisecond electrical pulses to the PN junction for phase transition facilitates the flexible field-programing of the MRRs' resonances. To the

Table 1 Performance comparison of various post-fabrication trimming methods

Ref	Technology	Tuning range > FSR	Bidirectional adjustability	Field programmable	Tunning time	Modulation/detection rates
This work	PCM	√	√	√	Milliseconds	4 × 100 Gb/s
[18]	Ion implantation	√	×	√	Seconds	—
[27]	Continuous laser	×	×	×	Hours	—
[30]	Femtosecond laser	×	√	×	—	—
[32]	polymer cladding	×	×	×	—	—

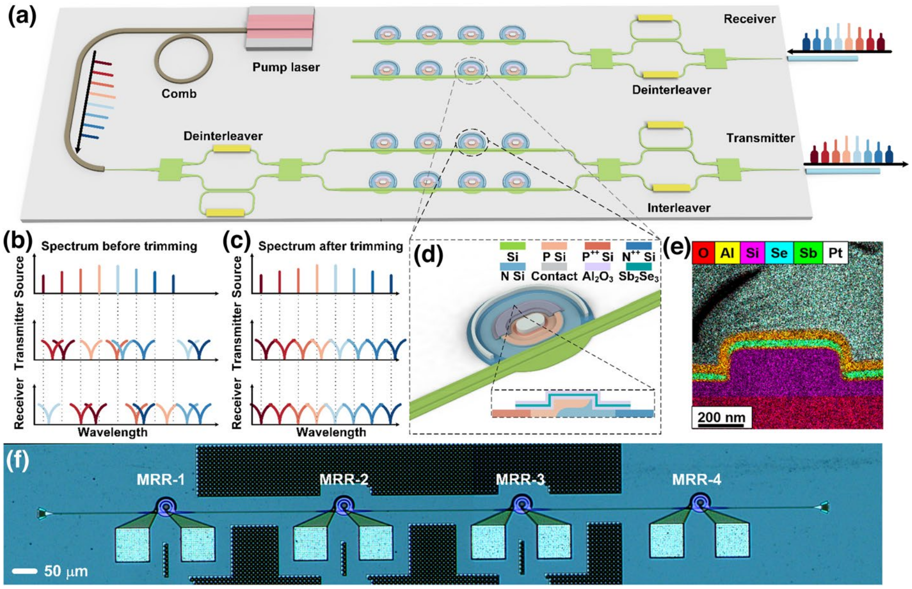

Fig. 1 PCM-powered MRR-based transceiver structure and principal. **a** Schematic of the MRR-based transceiver integrated with PCMs. **b**-**c** The comb, transmitter, and receiver spectrum (**b**) before and (**c**) after MRRs'resonance wavelength non-volatile trimming, respectively. **d** Detailed structure of the MRR integrated with SbSe patch. **e** EDS mappings of the SbSe-Si heterogeneous phase shifter cross-section. The distribution areas of Se and Sb overlap in the figure. **f** Microscope image of the fabricated four MRRs in cascade

best of our knowledge, it is the first demonstration of non-volatile field programming and post-fabrication wavelength trimming for silicon MRR-based transceivers using low-loss-PCM.

Results

Transceiver architecture

Figure 1(a) shows the schematic of the silicon PN junction MRR-based WDM transceiver integrated with the SbSe for non-volatile resonance wavelength reconfiguration and trimming. Kerr soliton combs provide on-chip multi-wavelength light sources, while a de-interleaver/interleaver pair are used to realize wavelength multiplexing and diminish modulation crosstalk [9]. Designated MRRs with aligned wavelength channels function as modulators and photodetectors specifically for the transmitter and receiver. The implementation of MRRs embedded with PN junction simplifies the design and fabrication of the transceivers for large-capacity high-density optical interconnect. However, fabrication errors will inevitably lead to a misalignment of the spectra among the source, transmitter, and receiver, thereby impairing the transmission performance, as depicted in Fig. 1(b). Using the SbSe-Si heterogeneous waveguide for spectral trimming can successfully realign the spectra of both the transmitter and the receiver with that of the source, ensuring the transceiver optimal functionality, as illustrated in Fig. 1(c). After the alignment of all wavelength channels, one of the MRRs can be used to monitor the intracavity power and realize simultaneous feedback control of all the MRRs against the environmental temperature perturbation by using a TEC.

Figure 1(d) shows the schematic diagram of the non-volatile MRR embedded with PN-junction. The MRR has a radius of 13 μm. An S-shaped PN junction is embedded in the waveguide with the P-type and N-type light doping concentrations of 2.3×10^{18} cm^{-3} and 3×10^{18} cm^{-3}, respectively. The PCM film covers half of the microring to form an SbSe-Si heterogeneous waveguide phase shifter for resonance wavelength trimming. An Al_2O_3 thin film is embedded between the PN junction and the PCM to realize electrical insulation so that the phase change of the PCM would not influence the electrical performance of the PN junction. Besides, the PCM is encapsulated by another Al_2O_3 thin film for material protection. Detailed design and simulation of the MRRs and the PN-junction can be seen in Supplementary Notes 1 and 2. The embedded S-shaped PN junction in the MRRs has three functions: (1) modulates the optical signal by altering the effective refractive index of the waveguide under a lower reverse bias; (2) facilitates in-microresonator photodetection at a higher reverse bias through photon-assisted tunneling [50]; (3) works as a microheater to trigger the phase change of SbSe via forward biased electrical pulses. For a proof-of-concept demonstration, we design and fabricate a non-volatile four-cascaded silicon MRR-based transceiver, and the fabricated four-cascade MRRs'microscope image is shown in Fig. 1(f). Figure 1(e) shows the energy dispersive spectroscopy (EDS) mappings of the fabricated SbSe-Si phase shifter.

Single MRR characterization

The as-fabricated SbSe-Si heterogeneous integrated PN-junction MRR was at the crystalline state. The amorphization process was realized by applying a short and intense electrical pulse with 10 V amplitude and 500 ns width to the PN junction, leading to the blueshift of the resonance wavelength, as shown in Fig. 2(a). For recrystallization, a relatively long and low pulse with 3 V amplitude and 1 ms width was applied to keep the temperature of SbSe between its crystallization temperature (200 ℃) and melting temperature (620 ℃). As shown in Fig. 2(b), the resonance wavelength is redshifted. We notice that the resonance wavelength does not return to the initial state due to the stochastic nature of the phase transition process and the resulting local non-stoichiometry [51, 52].

For the wavelength trimming, it is essential to realize fine-tuning and also a wide tuning range. The amorphization process requires melting of the PCM, so switching the phase state alters the film morphology, potentially causing the micro-ring resonance peak to deviate from the initial position. It is challenging to repeatedly tune the resonance peak over a large wavelength range using one pulse. However, the resonance wavelength can be gradually adjusted to the target position by precisely controlling the pulse energy. Figure 2(c) shows the tuning capability of the non-volatile MRR with the

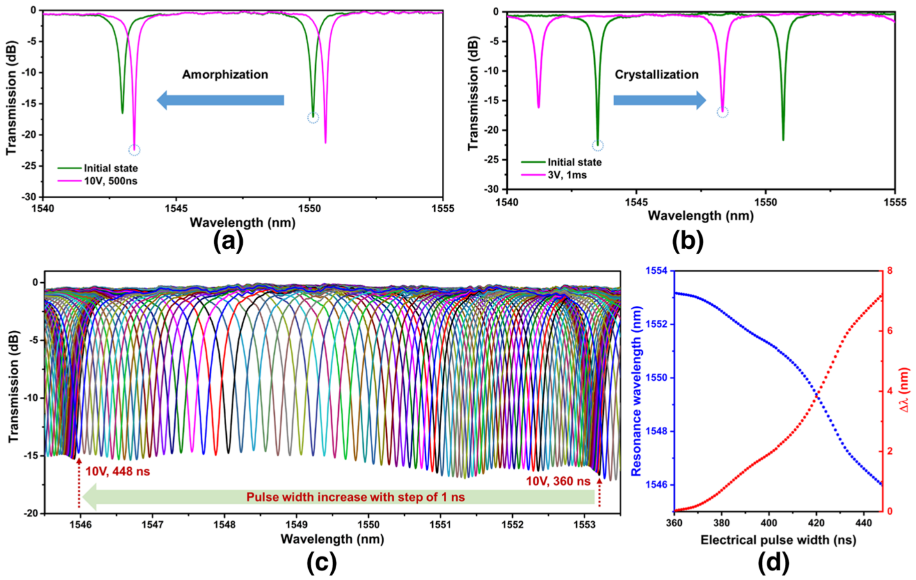

Fig. 2 Non-volatile wavelength tuning of the MRR integrated with the SbSe patch. **a**-**b** Transmission spectra of the device after the (**a**) amorphization and (**b**) crystallization processes, respectively. **c** Fine-tuning the resonance wavelength in one FSR by gradually increasing the electrical pulse width with 1 ns step during the amorphization process. **d** Extracted resonance wavelength shifts versus electrical pulse width

resonance tuned over one FSR. The electrical pulses had an identical amplitude of 10 V, while the pulse width was gradually increased from 360 to 447 ns with a tuning step of 1 ns. Figure 2(d) shows the extracted resonance wavelength upon the different electrical pulse widths. The resonance wavelength is tuned from 1553.21 nm to 1545.97 nm with a minimum tuning resolution of ~10 pm. The fine-tuning of the MRR resonance wavelength with over one FSR by just tuning the electrical pulse widths means that we can flexibly control and reconfigure the resonance wavelength using the phase change process, which is a superior option for post-fabrication wavelength trimming. The constancy of the resonance wavelength upon the cessation of the electrical pulse demonstrates the non-volatile nature of the resonance wavelength tuning (Supplementary Note 3). We also test its repeatability (Supplementary Note 4). Although the cyclicity and the tuning consistency of the SbSe PCM are still limited due to the material deformation, degradation, and stochasticity of phase transition processes [45, 52, 53], for the wavelength trimming, we can tune the resonance by a sequence of small pulses to approach the target wavelength. Besides, we don't need to frequently reconfigure the resonance wavelengths using the PCM, thereby the proposed scheme based on heterogeneous integrated low-loss PCM is sufficient for post-fabrication wavelength trimming.

We also characterized the MRR modulation and detection performance before and after the phase change of the PCM. Figures 3 (a) and (b) depict the spectra of a single MRR at various bias voltages before and after resonance wavelength trimming, respectively. After the SbSe amorphization process, the MRR resonance wavelength blue shifts from 1554.36 nm to 1552.65 nm without bias voltage. The static extinction ratio (ER) exhibits a mere 0.6 dB decrement from 14.2 dB and 13.6 dB. Figure 3(c) displays the derived modulation efficiency and quality factor (Q-factor) before and after the phase change. At −4 V bias voltage, the modulation efficiency is ~0.71 V • cm, and the

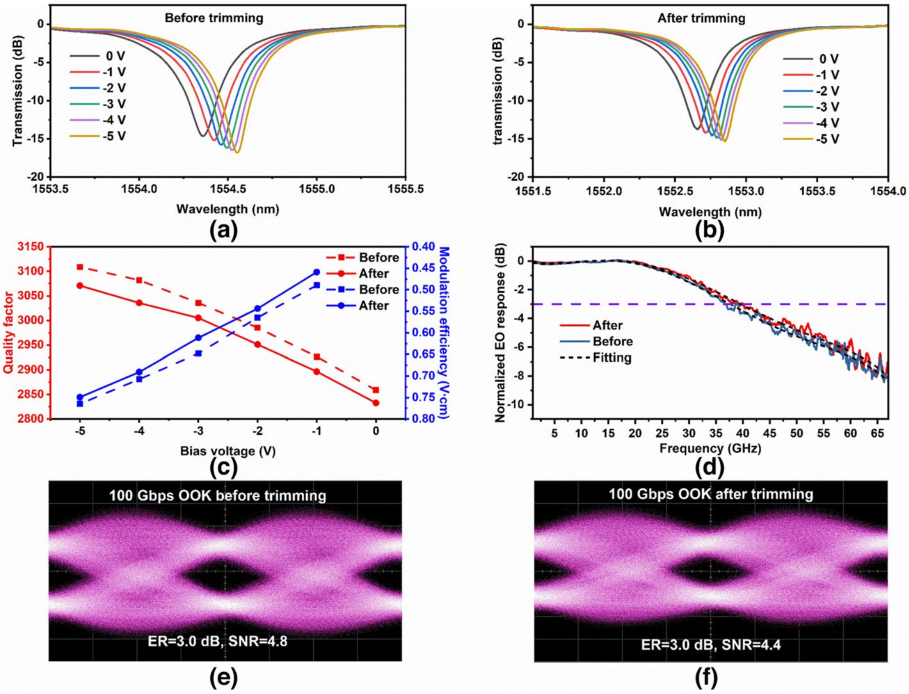

Fig. 3 Modulation performance of the MRR integrated with SbSe patch. **a**-**b** Transmission spectra **a** before and **b** after resonance wavelength post-fabrication trimming at various bias voltages. **c** Extracted Q-factor and modulation efficiency versus bias voltage. **d** Normalized EO response, and (**e**)-(**f**) 100 Gbps OOK modulation eye diagrams of the MRR (**e**) before and (**f**) after resonance wavelength trimming, respectively

Q-factor is ~3080 before trimming. A Q-factor variation of less than 50 is attributed to the increased optical loss of the SbSe patch due to deformation during the melting of the PCM [45]. The modulation efficiency is increased by less than 0.04 V·cm after amorphization, which may be due to the slight variation of the optical mode field profile upon phase change. Figure 3(d) shows the measured electro-optic (EO) bandwidth of the single MRR. After resonance wavelength trimming, the EO bandwidth increases from 37.6 GHz to 39.6 GHz. The slightly increased EO bandwidth after trimming is attributable to the reduced Q-factor. Figure 3 (e) and (f) display the measured 100 Gbps OOK modulation eye diagrams of the single MRR before and after resonance wavelength trimming. See supplementary note 5 for details on the measurement. The ER of the eye diagrams remains constant before and after resonance wavelength trimming, whereas the signal-to-noise ratio (SNR) slightly declines by 0.4.

Figure 4 compares the photodetection performance before and after resonance wavelength trimming for the silicon MRR embedded with the PN junction. The total and dark current of the MRR-based photodetector gradually increases with the bias voltage. At a bias of −8.4 V, the dark current is 1.00 µA. The total current is 2.44 µA for an input optical power of −6.85 dBm into the waveguide before the MRR resonance wavelength adjustment. The corresponding responsivity is 6.97×10^{-3} A/W. After the MRR resonance wavelength adjustment, the dark current and total current of the MRR-based photodetector are 1.19 µA and 2.69 µA, respectively, and the responsivity is 7.26×10^{-3} A/W. Thus, the dark current and responsivity of the MRR-based photodetector remain substantially constant, irrespective of the resonance wavelength adjustment process.

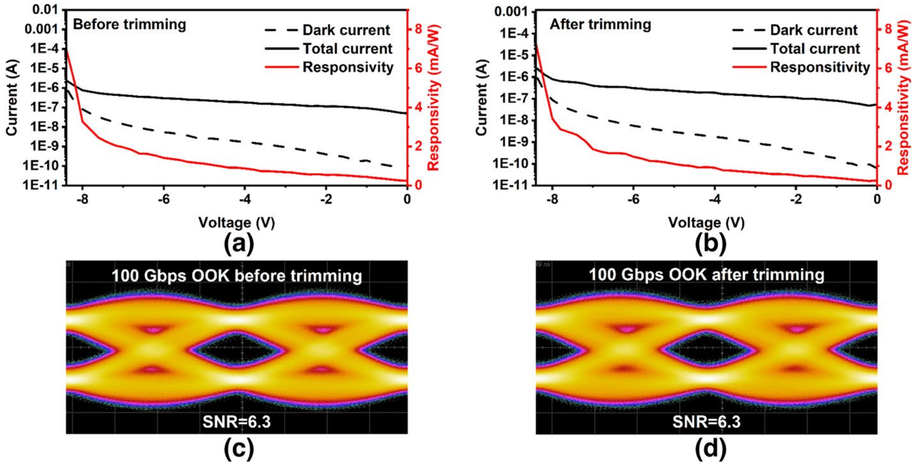

Fig. 4 Photodetection performance of the MRR integrated with SbSe patch. **a**-**b** Measured dark current, total current, and responsivity of the MRR-based photodetector at input optical power of −6.85 dBm (**a**) before and (**b**) after the trimming. **c**-**d** Measured 100 Gbps OOK of the MRR-based photodetector (**c**) before and (**d**) after the phase change

The 100 Gbps OOK eye diagrams of the MRR-based photodetector before and after the phase change are depicted in Figs. 4(c) and (d), respectively. See supplementary note 6 for measurement details. The eye diagrams of both cases exhibit an SNR exceeding 6.0. The SNR of the eye diagrams of the MRR-based photodetectors remains constant before and after the resonance wavelength trimming.

Benefitting from the insulator layer between the PCM and the PN junction in the MRR, the resonance wavelength trimming process has minimal impact on the MRR modulation and detection performance. In addition, regardless of whether the MRR performs as a modulator or photodetector, its resonance wavelength remains unchanged before and after modulation or detection, as shown in supplementary note 7, indicating the SbSe patch state will not be affected by the heat generated in the modulation or detection process.

Performance of four-channel non-volatile MRR-based transceivers

We further extended the single non-volatile MRR to a four-cascaded MRR array for potential WDM high-speed transceiver application. Upon identical MRR design, the initial resonance peaks of the four MRRs are squeezed together in the transmission spectrum, as shown in Fig. 5(a). The FSR of the four MRRs is 7.2 nm. Through adjusting PCM states, we individually fine-tuned the resonance wavelengths of the cascaded MRRs to achieve a uniform distribution across the FSR. Upon applying several amorphization electrical pulses with increased pulse widths, the resonance wavelength was gradually blue-shifted and adeptly aligned to the desired one. We adjusted the MRRs one by one. Figure 5(b) shows the uniformly distributed transmission spectrum of the four cascaded MRRs after resonance wavelength post-trimming. The resonance wavelength of each ring is illustrated. Subsequently, 4 × 100 Gbps OOK modulation and detection were demonstrated, as shown in Figs. 5(c) and (d). The ER and SNR of the four MRRs'modulation eye diagrams exceed 5.0 dB, and the SNR of the four MRRs'detection

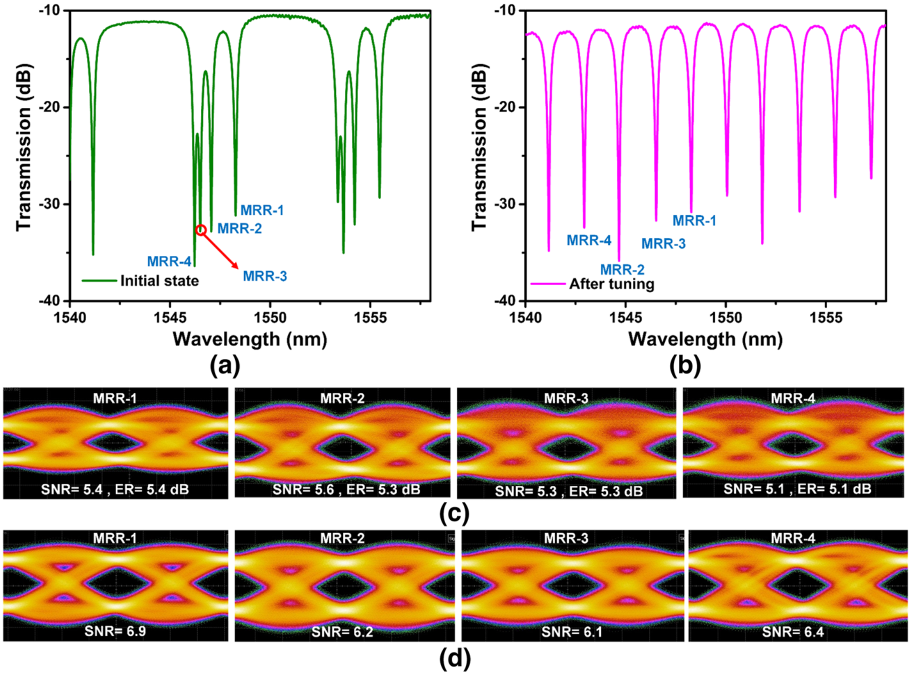

Fig. 5 Four-cascaded MRRs for modulation and detection. **a** Initial transmission spectrum. **b** Final transmission spectrum after resonance wavelength trimming. **c- d** Measured 100 Gbps OOK eye diagram of the four-cascaded MRRs when working as (**c**) modulators and (**d**) photodetectors, respectively

eye diagrams surpasses 6.0 dB. The successful calibration of the resonance wavelengths and the well modulation and detection performance consistency of the cascaded four MRRs further underscore the flexibility and scalability inherent in the proposed non-volatile MRR-based transceivers.

Due to the relatively large thermo-optic coefficient of Si, the working state of MRRs is sensitive to the environmental temperature variation. The measured temperature sensitivity of our MRRs is 0.077 nm/K and 0.078 nm/K before and after SbSe deposition, respectively, indicating that the SbSe has little influence on the thermal sensitivity of the MRRs (see Supplementary Note 8). Although we can realize post-fabrication trimming using the low-loss SbSe PCM, it is also important to realize a stable working state against temperature perturbation for practical applications. Therefore, we propose a feedback control scheme to realize stable modulation using a TEC. The experimental setup is shown in Fig. 6(a), given the maximum distance between the first and fourth MRRs is only ~ 950 μm, the resonance wavelengths of these two MRRs exhibit an almost synchronized variation to the ambient temperature change. Consequently, we harness the fluctuations in the photocurrent detected by the fourth MRR to appraise the spectral shifts occurring within the first MRR. The detected photocurrent change serves as a feedback mechanism to modulate the temperature of the TEC beneath the chip, thereby achieving precise thermal control of the first MRR.

In this proof-of-concept experiment, we turned on a high-power heat lamp which was placed about 1 m away from the setup to introduce the environmental temperature variation. After turning on the lamp, the ambient temperature increased by 2.3 C in 9.8 min. In the experiment, we first turned on the lamp to increase the ambient temperature and

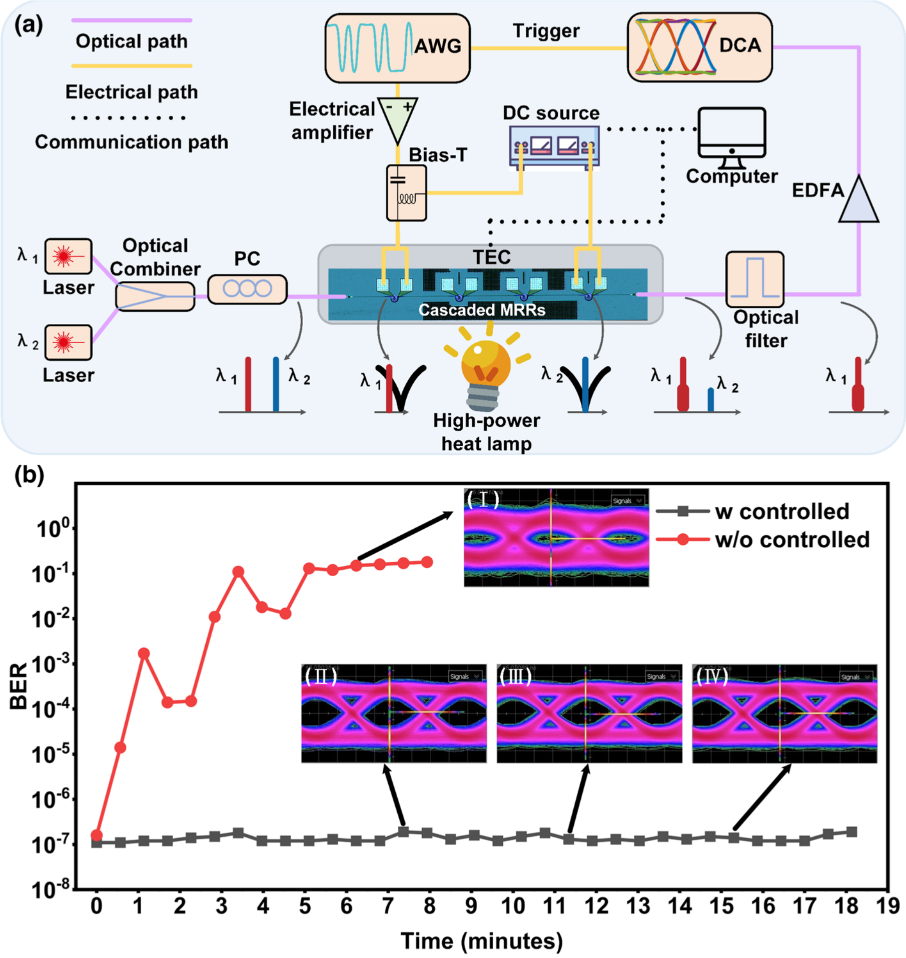

Fig. 6 Temperature feedback control using an on-chip MRR-based power meter. **a** Experimental setup of the feedback control scheme. AWG: arbitrary waveform generator; PC: polarization controller; TEC: thermoelectric cooler; EDFA: Erbium-doped fiber amplifier; DCA: digital communication analyzer. **b** BER of the 25 Gbps OOK modulation signal with and without thermal control. Insets (I)-(IV) are the corresponding eye diagrams

then turned off the lamp to allow the ambient temperature to decrease. We evaluated the bit error ratio (BER) of 25 Gbps OOK modulation received by a digital communication analyzer (DCA). See methods for detailed experimental description. Figure 6(b) shows the measured BER and the eye diagrams. Without the thermal feedback control, the BER of the modulated signal increases rapidly with time. Besides, the eye diagram deteriorates significantly within just ~6 min, as illustrated in the inset (I) of Fig. 6(b). When the control scheme is on, where the TEC temperature is adjusted according to the photocurrent detected by the fourth MRR, the BER of the 25 Gbps OOK modulation signal remains around 1×10^{-7}. Correspondingly, with thermal control, the eye diagram remains open and substantially stable over time, as depicted in the insets (II)-(IV) of Fig. 6. The successful thermal control experiments substantiate that the proposed scheme facilitates stable operation against room temperature fluctuation, dispensing with the need for an on-chip integrated heater. Since the Kerr microcombs can provide hundreds of wavelength channels, the requirement of an additional wavelength channel for on-chip state monitoring will not bring much complexity to the whole system.

Besides, we can simultaneously stabilize the working states of all the MRRs after the wavelength trimming by just using a TEC. This approach significantly diminishes the static power consumption associated with the thermal phase shifter and holds promise for application in large-scale photonic integrated circuits leveraging MRRs.

Discussion

To the best of our knowledge, the proposed scheme marks the pioneering application of low-loss SbSe PCM for the non-volatile resonance wavelength reconfiguration and trimming in silicon MRR-based transceivers. Owing to the non-volatile characteristic of SbSe, the trimming method ensures a permanent adjustment of the resonance wavelength with a minimal power consumption of 0.4 μJ and 5.8 μJ for the amorphization and crystallization processes, respectively (see Supplementary Note 4). Besides, benefiting from the low loss of the PCM and the Al_2O_3 insulation layer between the PCM and the PN junction, the MRR modulation and detection performance were negligibly impacted by the trimming process. By just varying the applied electrical pulse widths, we can precisely control the resonance wavelength of the MRR with a minimum tuning resolution of ~ 10 pm. The tuning range covers over one FSR. This simple electrical reconfiguration scheme makes it highly suitable for in-situ trimming and reconfiguration, compared with other post-fabrication trimming methods [18, 27]. Since the phase change of the SbSe patch is triggered by forward pulsing of the PN junction which is originally used for modulation and detection, a TiN phase shifter or a PIN diode can be left out and the PN junction can be embedded almost the whole circumference of the MRR, which is beneficial to improve the integration density and lowering the modulation voltages.

The MRR presented in this paper exhibits a responsivity of only ~ 0.007 A/W when functioning as a photodetector, attributed to the high doping concentration in the current design. This elevated doping results in a narrower depletion region, a diminished photon absorption region, and an increased dark current, collectively contributing to the reduced responsivity [7]. However, prior research has demonstrated that the responsivity of all-silicon photodetectors can be significantly enhanced through systematic optimization of MRR parameters, including resonator radius, doping concentration, mode-field overlap area, and Q-factor [6–8]. Moreover, the optoelectronic (OE) bandwidth of the MRR can be significantly improved by implementing a double-MRR structure [6]. Given that the integration of SbSe patches is predominantly facilitated by magnetron sputtering in the back-end of the line, the proposed methodology exhibits substantial potential for the wafer-scale fabrication of the non-volatile MRRs and holds excellent promise for application in the realm of large-scale high-density integration of MRR-based integrated circuits.

Conclusion

In summary, we proposed SbSe-Si heterogeneous integrated MRRs with non-volatile resonance wavelength reconfiguration for the large-capacity high-density WDM transceivers. We demonstrated a four-cascaded MRR array to show its performance. After resonance wavelength trimming with the SbSe PCM, the four MRRs' resonances were uniformly distributed in one FSR, and 4 × 100 Gbps OOK modulation and detection have been successfully realized. We also proposed a feedback scheme to realize stable modulation under ambient temperature variation by using one of the MRRs as a power meter. The experimental results indicate that the SbSe-integrated cascade MRR array can work well without the use of an on-chip integrated heater under ambient temperature change, effectively saving static power consumption. The proposed approach, which directly deposits the PCM onto the PN junction, leverages the existing modulation or detection pads to efficiently heat the PCM. This enables flexible tuning of the resonance wavelength of the MRR without increasing the chip footprint. The non-volatile nature of the PCM substantially reduces power consumption associated with wavelength tuning, and the relatively simple integration process facilitates wafer-level PCM implementation. Consequently, the scheme introduced in this paper holds significant potential for widespread adoption in large-scale MRR-based integrated optoelectronic circuits.

Methods

Fabrication of the silicon MRR embedded with PN-junction

The MRRs were first fabricated by Advanced Micro-foundry in Singapore including waveguide etching, doping, metallization, and oxide cladding. Besides, a standard oxide open process was applied to partially remove the oxide cladding and expose half of the microring waveguide. Subsequently, the fabrication of the PCM was done in the Center for Advanced Electronic Materials and Devices (AEMD) of SJTU. A 10-nm-thick Al_2O_3 layer was deposited using the Beneq Thermal/Plasma Enhanced Atomic Layer Deposition (ALD) system at 250 ℃, followed by a 30 nm thick SbSe film using a magnetron sputtering system (Denton Multi-target Magnetic Control Sputtering System) with an Ar flow rate of 25 sccm and an RF power of 80 W for 64 s. Another 40-nm-thick Al_2O_3 layer was deposited through the ALD. Finally, a window on the Aluminum pads was opened by e-beam lithography (EBL) and the chip was immersed in BOE for 30 s to remove the Al_2O_3 on the Aluminum pads and enable contact with test probes.

Feedback control experimental details

As shown in Fig. 6 (a), we employed an optical combiner to mix two laser beams with wavelengths of λ_1 and λ_2 before coupling them into the four cascaded MRRs. Specifically, the laser beam bearing the wavelength λ_1 is directed towards the first MRR for modulation, while the beam with wavelength λ_2 is guided to the fourth MRR for detection. The modulated signal, characterized by its wavelength λ_1, was directed through an optical bandpass filter to exclude any residual optical signals associated with wavelength λ_2 meticulously. Subsequently, the filtered signal was amplified by an EDFA and introduced into a DCA for BER floor assessment. We employed a high-power heat lamp to irradiate the chip to change the temperature in the chip vicinity. The AWG generated a 25 Gbps electrical OOK signal with an amplitude of 0.2 V_{pp}, which was subsequently amplified to achieve 2.8 V_{pp}. This amplified signal was then mixed with a −4 V DC bias voltage before being applied to the first MRR pad. Concurrently, a −6 V DC bias voltage was imposed on the fourth MRR to facilitate the collection of carriers generated within the depletion region of the S-shaped PN junction. The lasers, emitting at wavelengths λ_1 and λ_2, were operated at output powers of 13 dBm and 0 dBm, respectively. The first MRR operated at a 6 dB insertion loss on the blue side of the resonance peak for modulation, while the fourth MRR operated at a 10 dB insertion loss on the same side of its resonance peak. When fluctuations in ambient temperature occur, the resonance wavelength of the fourth MRR shifts, leading to variations in its detected photocurrent. Specifically, as room temperature rises (falls), the resonance wavelength undergoes a redshift (blueshift), causing the detected photocurrent to decrease (increase). To restore the resonance wavelength to its original state, the temperature of the TEC was adjusted downward (upward) accordingly. Specifically, the photocurrent generated by the fourth MRR is monitored using a precision current source (Keithley 2400). The MATLAB-based analysis then compares sequential photocurrent measurements and dynamically adjusts the TEC temperature in response to observed variations.

Abbreviations

MRR	Microring modulator
FSR	Free spectrum range
OOK	On–off keying
CMOS	Complementary metal-oxide semiconductor
PD	Photodetector
MZI	Mach–Zehnder modulator
PCM	Phase-change materials
ITO	Indium tin oxide
WDM	Wavelength-division multiplexing
TEC	Thermoelectric cooler
EDS	Energy dispersive spectroscopy
ER	Extinction ratio
Q-factor	Quality factor
EO	Electro-optic
SNR	Signal-to-noise ratio
DCA	Digital communication analyzer
BER	Bit error ratio
ALD	Atomic layer deposition
EBL	E-beam lithography

Supplementary Information

The online version contains supplementary material available at https://doi.org/10.1186/s43074-025-00174-7.

Supplementary Material 1.

Acknowledgements

Not applicable.

Authors' contributions

L. L. initiated the study and supervised the project with Y. L. and L. Z. S.R. conducted the simulations and layout design of the silicon MRR embedded with a PN junction. X.Y. performed the simulation and deposition of the PCM film. S.R., X.Y., and Z. L. collaboratively carried out the experimental testing. S. R. and X. Y. prepared the manuscript. All authors helped analyze the data. S.R., X.Y., Z. L., L. L., Y. L., J. C., N. W., M. Z., G. L., and L. Z. revised the manuscript.

Funding

This work was supported in part by the National Key R&D Program of China (2021YFB2801300), the National Natural Science Foundation of China (NSFC) (62135010, 62090052, 62305212), and the Shanghai Science and Technology Committee Rising-Star Program (23QA1404500).

Data availability

The data and materials that support the findings of this study are available from the corresponding authors upon request.

Declarations

Competing interests

The authors declare that they have no conflict of interest.

Received: 18 February 2025 Revised: 11 May 2025 Accepted: 16 May 2025

References

1. Shekhar S, Bogaerts W, Chrostowski L, et al. Roadmapping the next generation of silicon photonics. Nature Communications. 2024;15(1):751.
2. Wu H, Dai Q. Artificial intelligence accelerated by light. Nature. 2021;589(7840):25–6.
3. Ran S, Zhou G, Li Y, et al. Micro-ring modulators with integrated inductor to mitigate bandwidth and extinction ratio trade-off. IEEE Photon Technol Lett. 2024;36(4):231–4.
4. Yuan Y, Peng Y, Sorin WV, et al. A 5 × 200 Gbps microring modulator silicon chip empowered by two-segment Z-shape junctions. Nat Commun. 2024;15(1):918.
5. Xie C, Raj M, Joshi A, et al. A 64 Gb/s NRZ O-Band Ring Modulator with 3.2 THz FSR for DWDM Applications [Z]. Optical Fiber Communication Conference (OFC) 2024. 2024.https://doi.org/10.1364/OFC.2024.Tu2D.5
6. Peng Y, Yuan Y, Sorin WV, et al. An 8 × 160 Gb s−1 all-silicon avalanche photodiode chip. Nat Photon. 2024;18:928–34.
7. Zhang W, Zhu J, Li K, et al. Universal Silicon ring resonator for error free transmission links. Photonics Res. 2023;12(4):701–11.
8. Yuan Y, Sorin WV, Liang D, et al. Mechanisms of enhanced sub-bandgap absorption in high-speed all-silicon avalanche photodiodes. Photonics Res. 2023;11(2):337.
9. Rizzo A, Novick A, Gopal V, et al. Massively scalable Kerr comb-driven silicon photonic link. Nat Photon. 2023;17(9):781–90.
10. Rizzo A, Daudlin S, Novick A, et al. Petabit-scale silicon photonic interconnects with integrated kerr frequency combs. IEEE J Sel Top Quantum Electron. 2023;29(1):1–20.
11. Novick A, James A, Dai L Y, et al. High-bandwidth density silicon photonic resonators for energy-efficient optical interconnects. Appl Phys Rev. 2023, 10(4).
12. Liu Y, Zhang H, Liu J, et al. Parallel wavelength-division-multiplexed signal transmission and dispersion compensation enabled by soliton microcombs and microrings. Nat Commun. 2024;15(1):3645.
13. James A, Novick A, Rizzo A, et al. Scaling comb-driven resonator-based DWDM silicon photonic links to multi-Tb/s in the multi-FSR regime. Optica. 2023;10(7):832–40.
14. Omirzakhov K, Aflatouni F. 12.1 Monolithically Integrated Sub-63 fJ/b 8-Channel 256Gb/s Optical Transmitter with Autonomous Wavelength Locking in 45nm CMOS SOI [Z]. 2024 IEEE International Solid-State Circuits Conference (ISSCC). 2024: 218–20.https://doi.org/10.1109/isscc49657.2024.10454519.
15. Netherton A, Dumont M, Nelson Z, et al. 25.1 Short-Reach Silicon Photonic Interconnects with Quantum Dot Mode Locked Laser Comb Sources [Z]. 2024 IEEE International Solid-State Circuits Conference (ISSCC). 2024: 422–4.https://doi.org/10.1109/isscc49657.2024.10454400.
16. Levy CS, Xuan Z, Sharma J, et al. 8-λ × 50 Gbps/λ Heterogeneously Integrated Si-Ph DWDM Transmitter. IEEE J Solid-State Circuits. 2024;59:1–12.
17. Shi Y, Li X, Chen G, et al. Avalanche photodiode with ultrahigh gain–bandwidth product of 1,033 GHz. Nat Photon. 2024;18(6):610–6.
18. Jayatilleka H, Frish H, Kumar R, et al. Post-Fabrication Trimming of Silicon Photonic Ring Resonators at Wafer-Scale. J Light Technol. 2021;39(15):5083–8.
19. Zhang W, Ebert M, Li K, et al. Harnessing plasma absorption in silicon MOS ring modulators. Nat Photon. 2023;17(3):273–9.
20. Chan DWU, Wu X, Lu C, et al. Efficient 330-Gb/s PAM-8 modulation using silicon microring modulators. Opt Lett. 2023;48(4):1036–9.
21. Zhang Y, Zhang H, Zhang J, et al. 240Gb/s optical transmission based on an ultrafast silicon microring modulator. Photonics Res. 2022;10(4):1127–33.
22. Sakib M, Kumar R, Ma C X, et al. A 240 Gb/s PAM4 Silicon Micro-Ring Optical Modulator. 2022 Optical Fiber Communications Conference and Exhibition (Ofc), 2022.
23. Milosevic MM, Chen X, Yu X, et al. Ion Implantation of germanium into silicon for critical coupling control of racetrack resonators. J Light Technol. 2020;38(7):1865–73.
24. Milosevic MM, Chen X, Cao W, et al. Ion Implantation in silicon for trimming the operating wavelength of ring resonators. IEEE J Sel Top Quantum Electron. 2018;24(4):1–7.
25. Chen B, Yu X, Chen X, et al. Real-time monitoring and gradient feedback enable accurate trimming of ion-implanted silicon photonic devices. Opt Express. 2018;26(19):24953–63.
26. Lee H S, Kiravittaya S, Kumar S, et al. Local tuning of photonic crystal nanocavity modes by laser-assisted oxidation. Applied Physics Letters, 2009, 95(19).
27. Guo T, Zhang M, Yin Y, et al. A Laser-trimming-assist wavelength-alignment technique for silicon microdonut resonators. IEEE Photon Technol Lett. 2017;29(5):419–22.
28. Chen CJ, Zheng J, Gu T, et al. Selective tuning of high-Q silicon photonic crystal nanocavities via laser-assisted local oxidation. Opt Express. 2011;19(13):12480–9.
29. Bachman D, Chen Z, Prabhu AM, et al. Femtosecond laser tuning of silicon microring resonators. Opt Lett. 2011;36(23):4695–7.
30. Bachman D, Chen Z, Wang C, et al. Postfabrication phase error correction of silicon photonic circuits by single femtosecond laser pulses. J Light Technol. 2016;35(4):588–95.
31. Canciamilla A, Morichetti F, Grillanda S, et al. Photo-induced trimming of chalcogenide-assisted silicon waveguides. Opt Express. 2012;20(14):15807–17.
32. Lambert S, De Cort W, Beeckman J, et al. Trimming of silicon-on-insulator ring resonators with a polymerizable liquid crystal cladding. Opt Lett. 2012;37(9):1475–7.
33. Meng J, Gui Y, Nouri BM, et al. Electrical programmable multilevel nonvolatile photonic random-access memory. Light Sci Appl. 2023;12(1):189.
34. Chen R, Fang Z, Perez C, et al. Non-volatile electrically programmable integrated photonics with a 5-bit operation. Nat Commun. 2023;14(1):3465.

35. Delaney M, Zeimpekis I, Lawson D, et al. A new family of ultralow loss reversible phase-change materials for photonic integrated circuits: Sb2S3 and Sb2Se3. Adv Functional Mater. 2020;30:2002447.
36. Fang Z, Mills B, Chen R, et al. Arbitrary programming of racetrack resonators using low-loss phase-change material Sb2Se3. Nano Lett. 2023;24(1):97–103.
37. Fang Z, Chen R, Zheng J, et al. Ultra-low-energy programmable non-volatile silicon photonics based on phase-change materials with graphene heaters. Nat Nanotechnol, 2022.
38. Delaney M, Zeimpekis I, Du H, et al. Nonvolatile programmable silicon photonics using an ultralow-loss Sb2Se3 phase change material. Sci Adv. 2021;7(25):eabg3500.
39. Zhang H, Xu L, Chen J, et al. Ultracompact Si-GST hybrid waveguides for nonvolatile light wave manipulation. IEEE Photonics J. 2018;10(1):1–10.
40. Zheng J, Khanolkar A, Xu P, et al. GST-on-silicon hybrid nanophotonic integrated circuits: a non-volatile quasi-continuously reprogrammable platform. Optical Materials Express. 2018;8(6):1551.
41. Zhang C, Wei M, Zheng J, et al. Nonvolatile multilevel switching of silicon photonic devices with In2O3/GST segmented structures. Adv Optic Mater. 2023;11(8):2202748.
42. Xu P, Zheng J, Doylend JK, et al. Low-loss and broadband nonvolatile phase-change directional coupler switches. ACS Photonics. 2019;6(2):553–7.
43. Li X, Youngblood N, Ríos C, et al. Fast and reliable storage using a 5bit, nonvolatile photonic memory cell. Optica. 2018;6(1):1–6.
44. Zhang H, Zhou L, Xu J, et al. Nonvolatile waveguide transmission tuning with electrically-driven ultra-small GST phase-change material. Sci Bull. 2019;64(11):782–9.
45. Wu C, Yu H, Li H, et al. Low-loss integrated photonic switch using subwavelength patterned phase change material. ACS Photonics. 2018;6(1):87–92.
46. Ríos C, Zhang Y, Shalaginov MY, et al. Multi-level electro-thermal switching of optical phase-change materials using graphene. Adv Photonics Res. 2020;2:2000034.
47. Chen R, Fang Z, Fröch JE, et al. Broadband nonvolatile electrically controlled programmable units in silicon photonics. ACS Photonics. 2022;9(6):2142–50.
48. Xia J, Wang Z, Yang R, et al. Ultrahigh endurance and extinction ratio in programmable silicon photonics based on a phase change material with ITO heater. Laser Photonics Rev. 2024;18(4):2300722.
49. Wei M, Xu K, Tang B, et al. Monolithic back-end-of-line integration of phase change materials into foundry-manufactured silicon photonics. Nat Commun. 2024;15(1):2786.
50. You JB, Kwon H, Kim J, et al. Photon-assisted tunneling for sub-bandgap light detection in silicon PN-doped waveguides. Opt Express. 2017;25(4):4284–97.
51. Teo TY, Krbal M, Mistrik J, et al. Comparison and analysis of phase change materials-based reconfigurable silicon photonic directional couplers. Optical Mater Express. 2022;12(2):606–21.
52. Zhang Y, Ríos C, Shalaginov M Y, et al. Myths and truths about optical phase change materials: a perspective. Appl Phys Lett. 2021, 118(21).
53. Yang X, Nisar MS, Yuan W, et al. Phase change material enabled 2 x 2 silicon nonvolatile optical switch. Opt Lett. 2021;46(17):4224–7.

Publisher's Note